



Article

Tailorable Electronic and Electric Properties of Graphene with Selective Decoration of Silver Nanoparticles by Laser-Assisted Photoreduction

Inseon Song ¹, Yujeong Kim ¹, Byung Hoon Lee ², Minji Chae ¹, Sooyeon Kim ¹, ChangKyu Yoon ^{3,4} , Min-Kyu Joo ^{1,4} , Jeeyoung Shin ^{3,4}, Soo Min Kim ^{5,*} and Changhyun Ko ^{1,4,*}

¹ Department of Applied Physics, College of Engineering, Sookmyung Women's University, Seoul 04310, Korea

² Center for Integrated Nanostructure Physics (CINAP), Institute for Basic Science (IBS), Sungkyunkwan University, Suwon 16419, Korea

³ Department of Mechanical Systems Engineering, Sookmyung Women's University, Seoul 04310, Korea

⁴ Institute of Advanced Materials and Systems, Sookmyung Women's University, Seoul 04310, Korea

⁵ Department of Chemistry, Sookmyung Women's University, Seoul 04310, Korea

* Correspondence: soominkim@sookmyung.ac.kr (S.M.K.); cko@sookmyung.ac.kr (C.K.)

Abstract: While graphene shows great potential for diverse device applications, to broaden the scope of graphene-based device applications further, it would be necessary to tune the electronic state of graphene and its resultant electrical properties properly. Surface decoration with metal nanoparticles is one of the efficient doping methods to control the properties of two-dimensional materials. Here, we report the p-type doping effects in single-layer graphene decorated with silver nanoparticles (AgNPs) that were formed area-selectively by the facile one-step photoreduction (PR) process based on focused-laser irradiation. During the PR process, AgNPs were reduced on graphene in AgNO₃ solution by laser-driven photoexcitation followed by chemical reactions. Based on scanning electron microscopy analyses, the morphology characteristics of AgNPs were shown to be modulated by the laser dwell time and power controllably. Further, p-type doping effects were demonstrated using graphene-field-effect transistor structures whose graphene channels were selectively decorated with AgNPs by the PR process, as validated by the decrease in channel resistance and the shift of the Dirac point voltage. Moreover, the growth of AgNPs was observed to be more active on the graphene channel that was laser-annealed ahead of the PR process, leading to enhancing the efficiency of this approach for altering device characteristics.

Keywords: graphene; two-dimensional material; silver nanoparticle; photoreduction; field-effect transistor; doping effects



Citation: Song, I.; Kim, Y.; Lee, B.H.; Chae, M.; Kim, S.; Yoon, C.; Joo, M.-K.; Shin, J.; Kim, S.M.; Ko, C. Tailorable Electronic and Electric Properties of Graphene with Selective Decoration of Silver Nanoparticles by Laser-Assisted Photoreduction.

Nanomaterials **2022**, *12*, 3549.

<https://doi.org/10.3390/nano12203549>

nano12203549

Academic Editor: Filippo Giubileo

Received: 20 September 2022

Accepted: 6 October 2022

Published: 11 October 2022

Publisher's Note: MDPI stays neutral with regard to jurisdictional claims in published maps and institutional affiliations.



Copyright: © 2022 by the authors. Licensee MDPI, Basel, Switzerland. This article is an open access article distributed under the terms and conditions of the Creative Commons Attribution (CC BY) license (<https://creativecommons.org/licenses/by/4.0/>).

1. Introduction

Graphene, a monatomic sheet of a honeycomb crystal structure composed of sp²-hybridized carbon atoms, has been studied extensively for a couple of decades since it does not only show fundamentally unique phenomena including unordinary valley structures and quantum Hall effects [1] but it also has many beneficial physical properties such as ultrahigh charge carrier mobility [2], superb mechanical strength and elastic modulus [3,4], high transparency [5], etc., leading to a variety of potential applications such as electronic and optoelectronic devices [6–9], electrical energy storage [10], flexible electronics [11], metastructures [12], and so forth. Particularly for electronic and optoelectronic graphene-based devices, to broaden the scope of their applications further, it is highly required to tune the carrier concentration and majority carrier type of graphene, as the doping level of conventional semiconductors should be tailored in a wide range to meet the differing needs of contemporary electronics and optoelectronics [13].

From this perspective, although it is quite challenging to control the electronic properties in two-dimensional (2D) structures, various approaches have been developed for

doping 2D materials such as substitutional doping [14,15], electrostatic gating [8], surface functionalization [16,17], gas adsorption [13], ion irradiation [18], intercalation [19,20], and so on. The growth of metal nanoparticles on the graphene surface is also one of the effective doping methods to modulate the electronic state of graphene properly via charge carrier transfer across metal/graphene interfaces [21]. Among various metal nanoparticles, due to the extraordinary physical and chemical properties of silver nanoparticles (AgNPs), the 0D/2D heterostructures of AgNPs/graphene have been employed for demonstrating diverse synergetic applications such as electrocatalysts [22–24], electrochemical energy storages and sensors [25], photodetectors [26], transparent conductive coatings [27,28], etc., as well as for exploring fundamental phenomena such as localized surface plasmon resonance [21,26,29]. Moreover, integrating AgNPs with graphene structures may be structurally suitable for flexible device applications [30–32]. Meanwhile, a few studies have reported that AgNP decoration induces n-type doping in graphene [21,26,29,33].

While AgNPs have been produced on graphene in various ways such as chemical reduction, gas phase synthesis, thin film deposition followed by heat treatment, etc. [21,22,25,26,29,34], to our knowledge, no previous study has been reported regarding AgNP decoration on graphene by the photoreduction (PR) process driven by laser irradiation. This method enables the formation of AgNPs on 2D materials controllably via modulating the laser processing conditions [35]. Recently, Y. Lee, et al. have demonstrated controllable p-type doping in 2D molybdenum disulfide (MoS_2), one of the highly attractive 2D semiconductor species, by AgNP decoration based on the laser-assisted PR method [35]. Since graphene is a gapless semi-metal, AgNP growth can be activated by direct photoexcitation more easily on graphene than on a 2D semiconductor. Further, by adopting a focused-laser beam as an irradiation source for the PR process, AgNPs can be selectively formed on a desired area of graphene [13,36]. This one-step process may even allow microscale complicated patterns of AgNPs to be written on graphene without any additional lithography and subsequent high-temperature annealing processes required for the conventional area-selective fabrication of AgNPs based on physical deposition techniques [13,26,35–38].

In this work, utilizing the facile one-step focused-laser-assisted PR process, p-type doping effects were achieved in graphene where AgNPs were synthesized area-selectively on its surface. It was shown that the morphology characteristics of AgNPs on graphene were adjustable by tuning the laser processing parameters. Adopting graphene-based field-effect-transistor (GFET) devices, we demonstrated that the electronic state and electrical characteristics of graphene could be modified properly by AgNP-decoration-driven p-type doping. In addition, it was also observed that focused-laser-assisted annealing on graphene in water, prior to the PR process, made the AgNP growth kinetics more active, resulting in a more significant alteration of the device characteristics.

2. Materials and Methods

2.1. Nanoparticle Synthesis and Characterization

As described schematically in Figure 1a, AgNPs were synthesized via the PR process on single-layer graphene films (GFs; purity: 97%, Graphene Supermarket, Ronkonkoma, NY, USA) grown by chemical vapor deposition on a Cu surface and transferred onto 285 nm-thick $\text{SiO}_2/\text{B-doped Si}$ substrates (resistivity: 0.001–0.005 $\text{ohm}\cdot\text{cm}$) with PMMA (polymethyl methacrylate). Laser illumination was applied to single-layer GFs submerged in 0.1 M AgNO_3 solution (AgNO_3 powder purity: >99%, Alfa Aesar, Haverhill, MA, USA). Under the laser illumination, free-electron-hole pairs were generated by laser-assisted photoexcitation, and then Ag ions were reduced to Ag in the form of particles on the graphene surface by accepting the free electrons, releasing oxygen gas molecules [39]. Then, to remove solution residue, the samples were soaked in ultrapure water and then baked at 120 °C for 10 min in air. Figure 1b schematically shows the PR process composed of the charge carrier transport, graphene/solution interfacial

charge transfer, and chemical reactions in view of the energy band diagram [40–43]. The chemical equations for the reactions involved in the PR process are as follows [39]:

- (1) Graphene (G) + $h\nu \leftrightarrow e^- (G) + h^+ (G)$,
- (2) $e^- (G) + AgNO_3 \leftrightarrow Ag@G + NO_3^-$,
- (3) $h^+ (G) + 1/2H_2O \leftrightarrow h^+ (G) + 1/2OH^- + 1/2H^+ \leftrightarrow 1/4O_2 + H^+$, and
- (4) Graphene (G) + $h\nu + AgNO_3 + 1/2H_2O \leftrightarrow Ag@G + 1/4O_2 + HNO_3$.

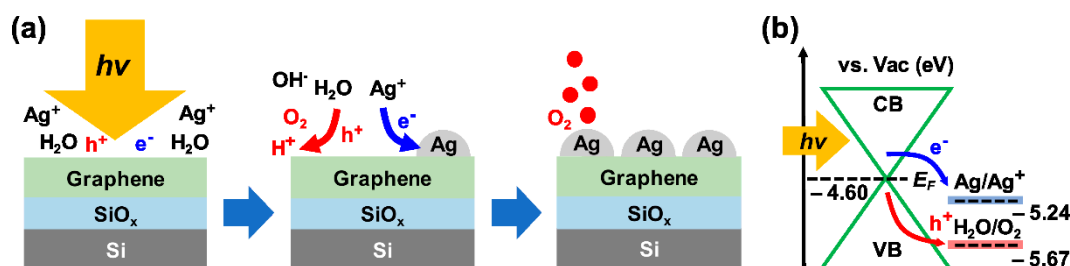


Figure 1. (a) Schematic drawing and (b) energy band diagram of the photoreduction (PR) process of silver nanoparticles (AgNPs) on graphene in the AgNO₃ solution. The electron energy levels are indicated with respect to the vacuum (Vac) level (i.e., in the absolute energy scale) [39–43].

Figure 2a shows a representative optical microscopy (OM) image taken from a GF decorated selectively with AgNPs by scanning a focused-laser beam in an area of $50 \times 50 \mu m^2$ on the GF in AgNO₃ solution at a laser power (P_L) of 5 mW for a laser dwell time (τ_L) of 2000 ms. As shown in Figure 2b, scanning electron microscopy (SEM) imaging showed that the nanoscale particles were distributed only over the laser-processed area. The elemental analysis based on energy-dispersive X-ray spectroscopy (EDS) combined with SEM imaging suggests that the nanoparticles were made of Ag. The details of the EDS analysis are summarized elsewhere (Figure S1).

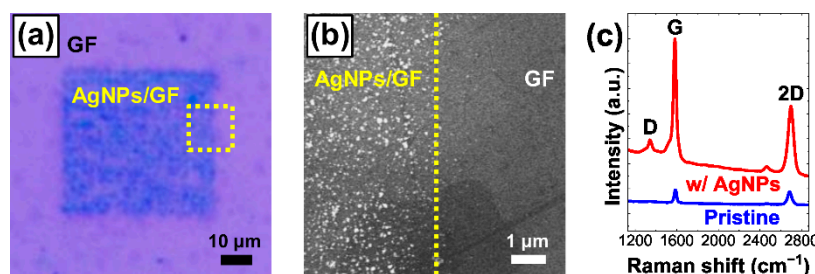


Figure 2. Representative images of AgNPs grown selectively on a graphene film (GF) taken by (a) optical microscopy (OM) and (b) scanning electron microscope (SEM), respectively. The area marked in the OM image (a) was scanned for the SEM image (b). (c) Raman spectra taken from the same spot of a GF with and without AgNPs [21,33].

Figure 2c includes typical Raman spectra acquired from the same spot of a GF before and after the AgNP decoration. The significant enhancement of the overall spectral intensity including 2D and G peaks may be due to the surface-enhanced Raman scattering (SERS) effects, which are well-known to be induced by localized surface plasmon resonances in metal nanoparticles [21,26,29,33,34]. The shift of the peak positions and the changes in the ratios of the peak intensities in Raman spectra represent the variations in microscopic aspects and internal stress states of the graphene as well as the doping effects of the AgNPs into the graphene [13,21,33,44–46]. Herein, the peak intensities of the D, G, and 2D bands were set as I_D , I_G , and I_{2D} respectively. The increase in the I_D/I_G intensity ratio by ~81.2% through the PR process indicated the creation of defects in the GF during the AgNP growth [13,21,33,44,45]. In addition, while the 2D and G peaks were blue-shifted by 17.6 cm⁻¹ and 1.7 cm⁻¹, respectively, the I_{2D}/I_G intensity ratio dropped by ~40.6%

representing simultaneous doping effects and structural disorder evolution [13,21,33,44,45]. In addition, the blue-shift of the 2D peak may also imply that tensile stress was applied in graphene upon the AgNP decoration [46]. However, no significant change in the Raman characteristics of the graphene was observed after only the focused-laser irradiation in water without AgNP-formation under the laser processing conditions used in this work. This implies that the focused-laser-irradiation itself may have not significantly resulted in microscopic structure change and defect creation in the graphene [13,21,33,44–46].

Both the focused-laser irradiation for the PR process and Raman spectroscopy experiments were carried out in the ambient conditions on a confocal Raman spectrometer system (XperRamCompact, NANOBASE, Seoul, Korea) equipped with objective lenses and a continuous-wave laser source of wavelength 532 nm. During the focused-laser irradiation, the laser beam diameter and raster step size were $\sim 5\ \mu\text{m}$ and $\sim 3\ \mu\text{m}$, respectively, and the P_L was set in the range from 2 mW to 30 mW (in the power density $\sim 0.14\ \text{MW}/\text{cm}^2$ to $\sim 2.04\ \text{MW}/\text{cm}^2$). The AgNP growth could be roughly localized down to the spot area of the laser beam (Figure S2). Raman spectra were measured using a laser beam focused to a laser beam diameter of $\sim 1\ \mu\text{m}$ at P_L of 1 mW (in the power density $\sim 1.70\ \text{MW}/\text{cm}^2$). The morphology of the AgNPs was observed in detail using SEM equipped with a field-emission gun as an electron source. (JSM-7600F, JEOL, Tokyo, Japan) and analyzed by the ImageJ software. EDS (X-Max, Oxford Instruments, Abingdon, UK) was also conducted for elemental analyses on the surface of AgNPs-decorated graphene using the field-emission electron source of the SEM operated at an accelerating voltage of 15 keV.

2.2. Field-Effect-Transistor Device Fabrication and Characterization

GFET devices were built through a series of conventional fabrication processes including photolithography, reactive ion etching with O_2 plasma, metallization, etc. Top metal electrodes of Cr/Au (thickness: $\sim 5\ \text{nm}/\sim 50\ \text{nm}$) were deposited onto the patterned graphene films by e-beam evaporation. Then, all the devices were annealed at $350\ ^\circ\text{C}$ for 15 min while the processing pressure was kept at $\sim 100\ \text{mTorr}$ using Ar gas whose flow rate was $\sim 0.5\ \text{sccm}$ (standard cubic centimeters per minute) in a rapid thermal annealing system. The GFET devices were back-gated across the $285\ \text{nm}$ -thick SiO_2 layers using the heavily p-doped Si substrates as the bottom electrodes during device characterization with a semiconductor device parameter analyzer (B1500A, Keysight, Santa Rosa, CA, USA) at room temperature and vacuum pressure of $\sim 3 \times 10^{-6}\ \text{Torr}$ in a vacuum probe station equipped with a turbo pump system. To explore the interactive effects of AgNPs on the electronic and electrical properties of graphene as well as the device characteristics of the GFETs, the device measurements were carried out before and after the selective synthesis of AgNPs via the PR process on the microscale graphene channels (GCs).

3. Results and Discussion

To investigate how the laser processing parameters affected the growth of the AgNPs, a series of PR experiments were carried out varying the P_L and τ_L . Then, the AgNPs/GF regions were observed by OM to roughly investigate how the growth of the AgNPs depended on the laser parameters. Selective OM images of the AgNPs/GFs prepared under different laser parameters can be found elsewhere (Figure S3). Then, the morphology and distribution of the AgNPs were probed more precisely through the use of SEM. Figure 3a–f displays a representative set of SEM images of the AgNPs/GF regions given by the PR process operated in the range of P_L from 2 mW to 30 mW for a τ_L of 500 ms. In addition, Figure 3b,g–i includes a series of typical SEM images taken from the AgNPs/GF regions prepared at a P_L of 5 mW in the range of τ_L from 500 ms to 2000 ms. For statistically reliable analyses of the morphology of the AgNPs, the surface coverage (θ) and average particle size (α) for each laser condition were determined by considering at least five SEM images taken from different AgNPs/GF regions of $3.5 \times 5\ \mu\text{m}^2$. Herein, α indicates the average diameter of the AgNPs calculated on the assumption that all particles were spherical.

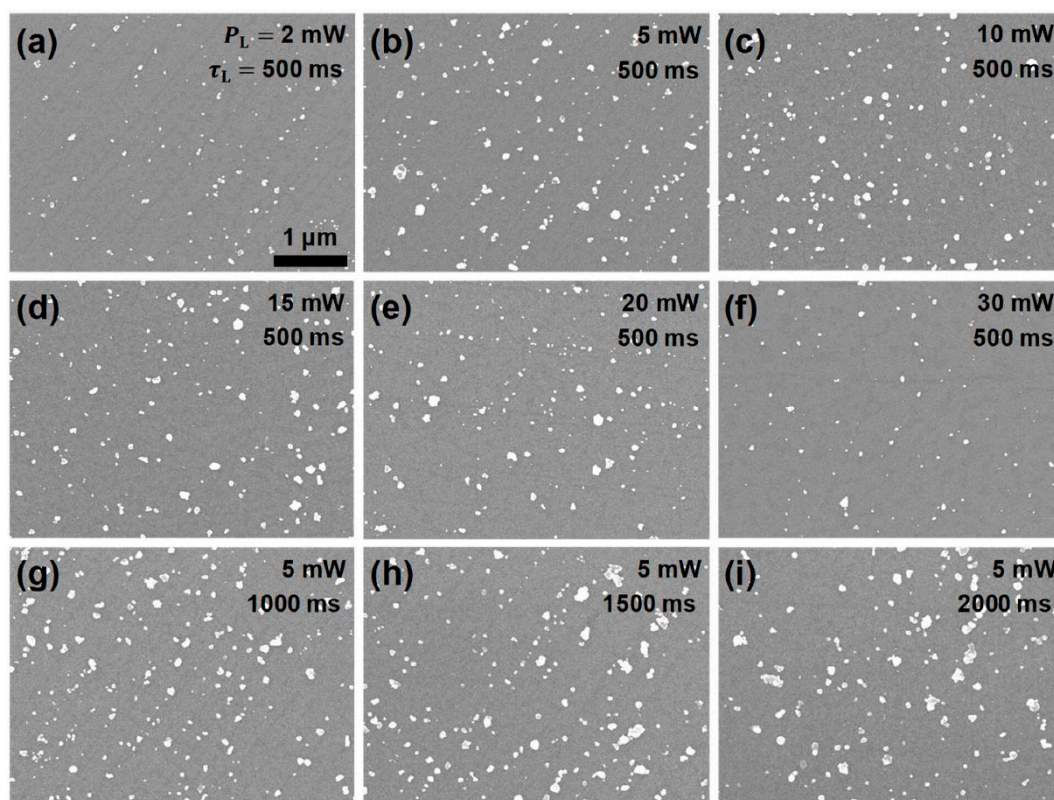


Figure 3. Representative SEM images taken from the regions of AgNPs/GF prepared by the PR process under various focused-laser irradiation conditions: for constant laser dwell time (τ_L) of 500 ms, at various laser powers (P_L s) of (a) 2 mW, (b) 5 mW, (c) 10 mW, (d) 15 mW, (e) 20 mW, and (f) 30 mW, and at a fixed P_L of 5 mW for varying τ_L s of (b) 500 ms, (g) 1000 ms, (h) 1500 ms, and (i) 2000 ms. All images are presented at the same scale.

Figure 4a–d exhibits that both of the θ and α of the AgNPs are affected by the P_L and τ_L in a complicated way. At the relatively low P_L of 5 mW or less, as expected, the AgNPs grew more as the P_L or τ_L increased controllably. However, it appeared that excessive laser illumination resulted in the degradation in AgNP growth probably since the reactions were hindered by the convection and evaporation of the solution more heavily with increasing P_L or τ_L . When the P_L was set as 20 mW, the AgNP growth was observed to be the most active at a τ_L of 1000 ms, while at 30 mW, the growth was quite suppressed in the overall range of τ_L . Although the laser conditions should have been optimized for growing the AgNPs efficiently, these results imply that, via controlling the laser parameters for the PR process, the growth kinetics of the AgNPs on graphene were delicately adjustable, leading to the detailed tunability of the electronic and electric properties of the AgNP-decorated graphene as well as the device characteristics of the GFETs. Due to the excellent electronic [2] and mechanical properties [3,4] of graphene, the GEET can be embedded into high-performance electronics [47], opto-electronics [26], sensors [48], as well as wearable devices [49].

To investigate how the properties of graphene were affected by the Ag decoration, GFET characterization was carried out at room temperature in conjunction with the PR experiments. Considering that the surface morphology deformation and coalescence of AgNPs are known to occur via surface diffusion actively above 200 °C, the structure of the AgNPs/GC and the GFET performance were expected to be stable under ordinary operational conditions [38,50,51]. The interactions between the GC and AgNPs were investigated by monitoring the device characteristics of the back-gated GFET structure based on a GC illustrated schematically in the side-view in Figure 5a. Figure 5b includes an OM plan-view image showing one of the typical GFET devices exploited in this study where both their channel widths and lengths were $\sim 60 \mu\text{m}$. The PR process was applied to the

two different GFET devices for selectively decorating the GCs with AgNPs in the area of $\sim 60 \times 30 \mu\text{m}^2$ at a P_L of 5 mW for a τ_L of 500 ms and 2000 ms, as shown in Figure 5c,d, respectively. Henceforth, the former was called dev1, while the latter was called dev2. The metal electrodes and channel regions near them were not laser-irradiated directly to avoid any damage to the devices. Consistently with the trend observed in Figure 4a–d, it is likely that, at this P_L of 5 mW, the longer τ_L led to controllably producing a larger amount of AgNPs in terms of the contrast of the OM images.

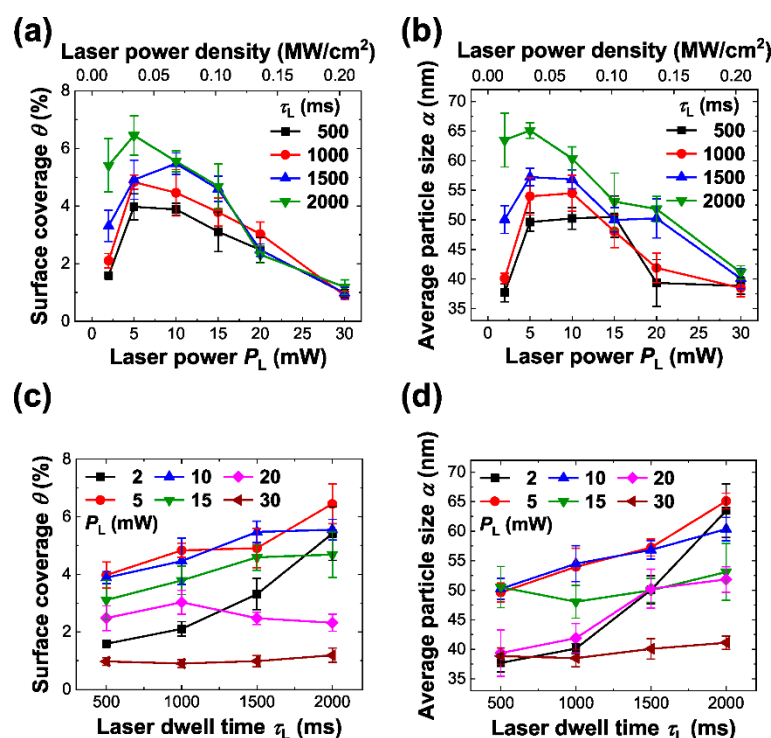


Figure 4. Morphology characteristics of AgNPs grown on a GF at varying laser parameters. (a) The surface coverage (θ) and (b) average particle size (α) of AgNPs are plotted as a function of P_L at various τ_L s. (c) The θ vs. τ_L and (d) α vs. τ_L plots are also given at several different P_L s. The error bars indicate the standard deviation.

Further, SEM was also performed on the AgNPs/GCs of dev1 and dev2 to evaluate the morphology of AgNP in more detail and understand their influence on the device characteristics. Figure 6 includes the two representative SEM images scanned from the AgNPs/GC regions of dev1 in Figure 5c and dev2 in Figure 5d. The AgNPs seemed to grow more actively on the patterned GCs than those on the GFs and the reasons are discussed later. Based on the SEM analyses, the θ & α values of the AgNPs on the GCs of dev1 and dev2 were estimated to be $\sim 6.34 \pm 0.25\%$ & $\sim 24.72 \pm 0.47$ nm and $\sim 6.77 \pm 0.32\%$ & $\sim 29.60 \pm 1.25$ nm, respectively. The α values of the AgNPs on the GCs were observed to be generally smaller than those on the GFs under the same laser conditions, whereas the θ values showed the opposite trend (Figure S4). From these results, it can be inferred that initial seeds for AgNP growth may exist more in fabricated GCs than in pristine GFs, as also confirmed by the comparison of the number of AgNPs.

As shown in Figure 7a, the drain current (I_{drain}) was measured as a function of the gate voltage (V_G) in the range of -50 V to $+50$ V at a drain-to-source voltage (V_{DS}) of 10 mV on dev1 before and after the AgNPs were decorated at a P_L of 5 mW for a τ_L of 500 ms. For comparison, Figure 7a also includes the I_{drain} vs. V_G plot for dev2 where the AgNPs/GC structure was prepared at the same P_L but for a longer τ_L of 2000 ms. Dev1 showed, with the as-fabricated GCs before AgNP decoration, typical ambipolar transport behavior with a small negative Dirac point voltage (V_{Dirac}) indicating that the GC of dev1 was lightly

n-doped in the initial stage. It should be noted that dev2 showed very similar $I_{\text{drain}} - V_G$ characteristics in the as-fabricated state to those of dev1 (data not shown here).

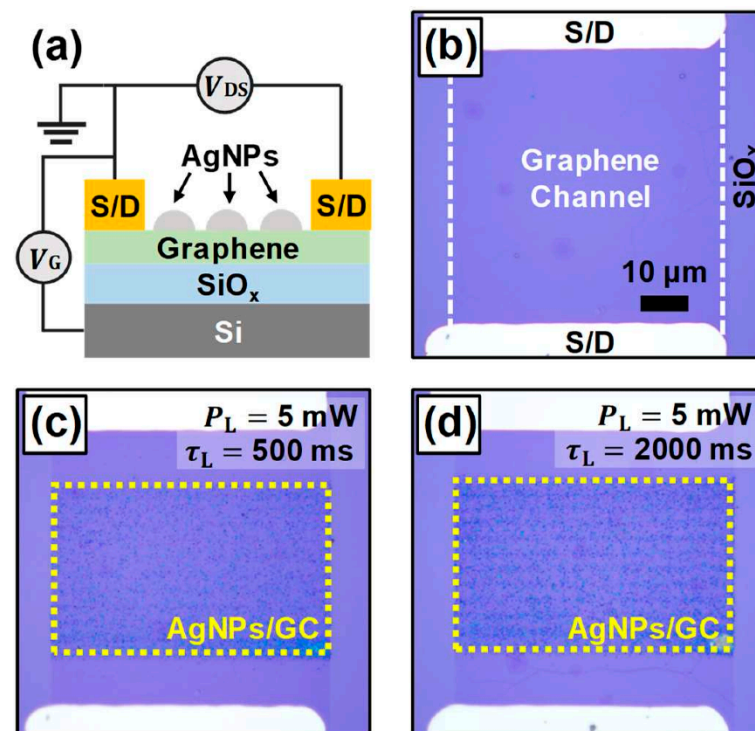


Figure 5. (a) Schematic side-view diagram of the graphene-based field effect transistor (GFET) device where the graphene channel (GC) surface is covered with AgNPs. OM plan-view images of the GFET devices with (b) an as-fabricated GC and two AgNP-coated GCs prepared differently at P_L of 5 mW for τ_L s of (c) 500 ms (dev1) and (d) 2000 ms (dev2), respectively. (b–d) Are displayed at the same scale.

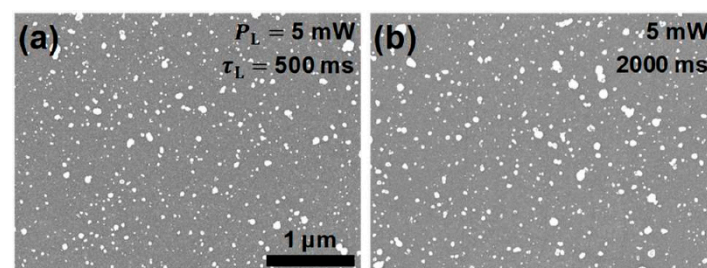


Figure 6. Selective SEM images of the regions of AgNP-decorated GCs. The AgNPs/GC regions in (a,b) were prepared by the PR process at P_L of 5 mW for τ_L s of 500 ms (dev1) and 2000 ms (dev2), respectively. Both images are displayed at the same scale.

In addition, the I_{drain} vs. V_{DS} curves were acquired in the range of V_{DS} from -50 mV to $+50$ mV at various V_G s for monitoring the V_G -dependent channel resistance (R) as well as evaluating the performance of the metal-graphene contacts. Figure 7b shows the selective three sets of the $I_{\text{drain}} - V_{\text{DS}}$ data at V_G of 0 and ± 50 V for each sample. It was clearly observed that the R varied with V_G and was influenced by the AgNP decoration, which was consistent with the $I_{\text{drain}} - V_G$ behavior shown in Figure 7a. Moreover, the linearity of the I_{drain} vs. V_{DS} plots validated the fact that the Ohmic contacts were created with negligible Schottky barrier heights across the metal-graphene interfaces of the GFETs throughout the operation. Considering the correlation between the AgNP morphology characteristics and device behavior, AgNPs formation seemed to enhance the channel current level, particularly in the regime below the V_{Dirac} where the holes were the dominant charge carriers along with the shift of V_{Dirac} in the positive direction of V_G .

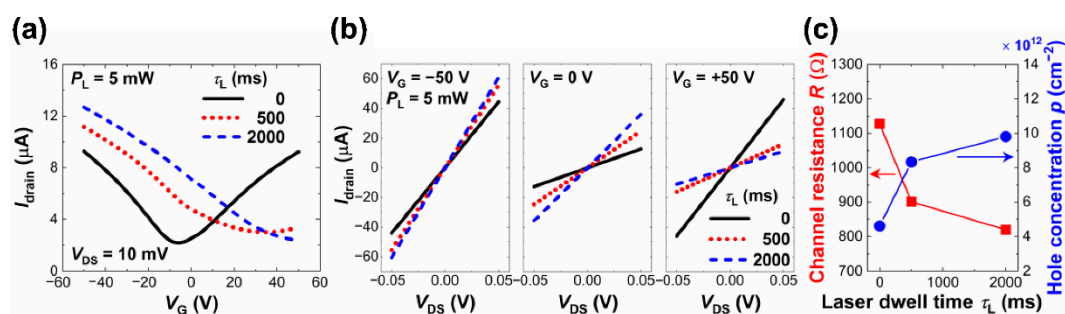


Figure 7. Variations in GFET device characteristics by AgNP decoration. (a) Drain current I_{drain} vs. gate voltage (V_G) curves measured at V_{DS} 10 mV on the GFETs based on GCs decorated without and with AgNPs prepared at P_L of 5 mW for varying τ_L s. (b) Three sets of I_{drain} vs. V_{DS} plots of the GFETs with and without AgNP decoration at V_G 0 and $\pm 50 \text{ V}$ for each. (c) The R and p at $V_G -50 \text{ V}$ as a function of the τ_L .

These p-type doping effects could be due to the possible transfer of charge carriers such as free electrons from the graphene to the AgNPs (or free holes in the opposite direction) and the resultant lowering of the Fermi energy level in the graphene. Previously, the n-type doping effects in graphene have been reported based on several AgNPs/graphene heterostructures created in different ways from that used in this work [21,26,29,33]. However, considering that the work function of Ag varies in the wide range from 4.14 eV to 4.81 eV due to many factors such as surface crystallographic orientation, crystal structures, synthesis methods, environmental conditions, etc., it is not surprising that p-type doping was achieved here [41,52–57]. In addition, the work functions of graphene and SiO_x are $\sim 4.60 \text{ eV}$ and $\sim 4.90 \text{ eV}$, respectively, and hence, the transfer of electrons from graphene to the SiO_x/Si substrate possibly contribute to the p-type doping effects [41,56,57]. Rather, the possibility of bidirectional doping with the same nanoparticle material would make this material system attractive for developing more advanced device structures on graphene such as photoactive p-n junctions [13].

As plotted in Figure 7c, the R values in the hole conduction regime at $V_G = -50 \text{ V}$ decreased by $\sim 20.1\%$ and $\sim 27.3\%$ via the AgNP decoration grown at a P_L of 5 mW for τ_L s of 500 ms and 2000 ms, respectively. Figure 7a shows that dev1 experienced a shift of V_{Dirac} of $\sim 40 \text{ V}$ in the positive direction of V_G and that of dev2 was even shifted over the upper limit of the V_G measurement range ($V_G = +50 \text{ V}$), confirming that the p-type doping effects became stronger in the graphene as more AgNPs were formed. The field-effect hole mobility (μ_p) of the GCs was also calculated as $\mu_p = Lg_m/WC_{\text{ox}}V_{\text{DS}}$, where W and L are both the width and length of the GCs, respectively, and were $\sim 60 \mu\text{m}$, C_{ox} is the oxide capacitance per area, and g_m is the slope of an I_{drain} vs. V_G plot in the linear region. The μ_p was observed to decrease with the amount of AgNPs on the GC surface represented by the α value; for dev1, from $\sim 1202.5 \text{ cm}^2/\text{V}\cdot\text{s}$ to $\sim 832.9 \text{ cm}^2/\text{V}\cdot\text{s}$ ($\sim 30.7\%$ decrease), while for dev2, $\sim 1236.1 \text{ cm}^2/\text{V}\cdot\text{s}$ to $\sim 777.9 \text{ cm}^2/\text{V}\cdot\text{s}$ ($\sim 37.1\%$). The hole carrier concentration (p), defined as the number of holes per unit area, was calculated in the hole conduction regime at $V_G = -50 \text{ V}$, where the holes were the majority of the carriers. Figure 7c shows that the p value was enhanced up to $\sim 104.3\%$ as the τ_L value increased to 2000 ms. Accordingly, it was inferred that the μ_p decreased as the carrier scattering limiting the carrier transport in the GCs became stronger upon the charge transfer from the AgNPs [13].

Moreover, we also tried a two-step process to prepare a AgNPs/GC where the first step was to apply focused-laser irradiation selectively onto a GC in water, excluding any PR-related chemical reaction, while the second step was, as previously performed, to grow AgNPs on the GC in AgNO_3 solution by the PR process in the same selective area. The GFET visualized in Figure 8a, called dev3 from now on, underwent the two-step process where both steps were selectively processed at a P_L of 5 mW for τ_L of 500 ms in an area of $\sim 60 \times 30 \mu\text{m}^2$.

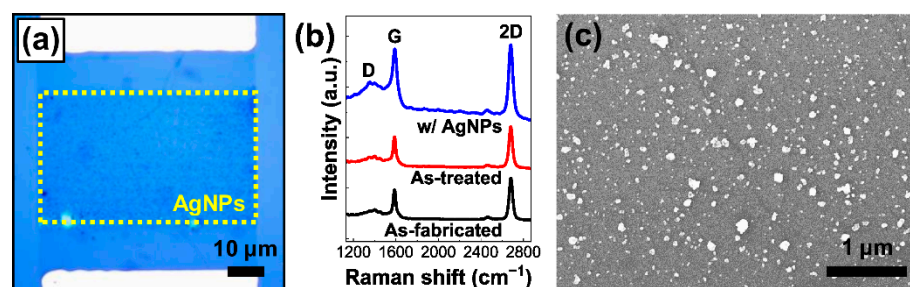


Figure 8. The two-step process composed of laser-irradiation treatment in water and PR-induced AgNP growth. (a) OM plan-view image of the GFET device based on a AgNPs/GC prepared by the two-step process (dev3). Both steps were carried out under the same laser conditions of $P_L = 5$ mW and $\tau_L = 500$ ms. (b) A set of representative Raman spectra taken from the GC of dev3 in the three states: (i) as-fabricated, (ii) as-treated just after the first step, and (iii) after the second step of AgNP decoration [21,33]. (c) A typical SEM image obtained from a AgNPs/GC region of dev3 in (a).

As summarized in Figure 8b, a set of Raman spectra was acquired from the three different GC regions of dev3: (i) as-fabricated, (ii) as-treated just after the first step, and (iii) AgNPs/GC given by the full process. In the comparison of the Raman spectrum taken from the pristine GF in Figure 2c, that of the as-fabricated GC in Figure 8b showed a clear signal of the D peak representing that the graphene seemed to become somehow defective through the device fabrication process [21,33]. The defect sites could act as the seeds for AgNP nucleation, probably leading to more active AgNP growth on the GCs than on the pristine GFs as can be seen above [58]. In addition, no significant change in the Raman characteristics by the first step in Figure 8b may only rule out the possibility of additional severe damage in the graphene by focused-laser irradiation in water and, more importantly, imply that the p-type doping in graphene was mainly due to the interaction with the AgNPs. After the second step, the I_D/I_G intensity ratio increased by $\sim 71.7\%$ while a decrease of $\sim 8.59\%$ in the I_{2D}/I_G intensity ratio was observed, indicating additional defect creation and p-type doping effects, respectively [13,21,33,44,45]. Further, an enhancement of the overall Raman spectral intensity was observed from the AgNPs/GC, similarly to the AgNPs/GF in Figure 2c [21,26,29,33,34]. More interestingly, it seems that the two-step process rendered the AgNP growth on the GC more active than the previous one-step process and, accordingly, more substantially enabled the tuning of the device characteristics of the GFETs by AgNP decoration.

Figure 8c shows a representative SEM image scanned from the AgNPs/GC region of dev3 in Figure 8a. By the SEM image analyses, the θ & α values of the AgNPs/GC of dev3 were given as $\sim 7.43 \pm 0.68\%$ & $\sim 32.70 \pm 1.46$ nm, respectively and they were much higher than those of dev1, i.e., $\sim 6.34 \pm 0.25\%$ & $\sim 24.72 \pm 0.47$ nm, respectively, prepared by the one-step method under the same laser conditions (Figure S4). Probably, the focused-laser treatment in water seemed to enable gentle defect generation as well as surface cleaning and, hence, facilitate more vigorous AgNP growth.

The tunable characteristics of the GFETs under the two-step process were investigated by measuring the $I_{\text{drain}} - V_G$ curve in the range of V_G from -50 V to $+50$ V at a V_{DS} of 10 mV as well as the $I_{\text{drain}} - V_{\text{DS}}$ data at a V_G of 0 and ± 50 V from dev3 in the three states of (i) as-fabricated, (ii) as-treated just after the first step, and (iii) AgNPs/GC prepared by the full process, as summarized in Figure 9a,b, respectively. For the comparison, Figure 9a,b also includes the characteristics plots of dev1 prepared by the one-step process at the same P_L and τ_L . Figure 9c shows that, by the first step, the R of dev3 decreased slightly by $\sim 7.41\%$ at $V_G = -50$ V, probably due to the gentle annealing effects driven by the focused-laser irradiation in water. These annealing effects probably enabled the removal of the factors that impair the carrier mobility, such as surface, interface contaminants, adsorbate gas molecules, etc. [59,60]. Then, the decrease in the R of dev3 at $V_G = -50$ V was estimated to be $\sim 28.8\%$ throughout the full two-step process, which was much larger than that of the

counterpart dev1 (~20.1%) and even that of dev2, which was prepared for a much longer τ_L of 2000 ms (~27.3%). In Figure 9b, the linearity of all the I_{drain} vs. V_{DS} plots represents that the quality of the Ohmic contacts were sustained well throughout the full two-step process. The V_{Dirac} of dev3 was observed to also be shifted in the positive direction of V_G , similar to dev1 and dev2. Figure 9c shows that p of dev3 reached $\sim 1.19 \times 10^{13} \text{ cm}^{-2}$ after the two-step process, which was higher than $\sim 8.33 \times 10^{12} \text{ cm}^{-2}$ of dev1 after the one-step process and even $\sim 9.80 \times 10^{12} \text{ cm}^{-2}$ of dev2. These results represent that the more active AgNP growth upon the two-step process brought about stronger p-type doping effects on the graphene and, accordingly, more significant modulation of the GFET characteristics.

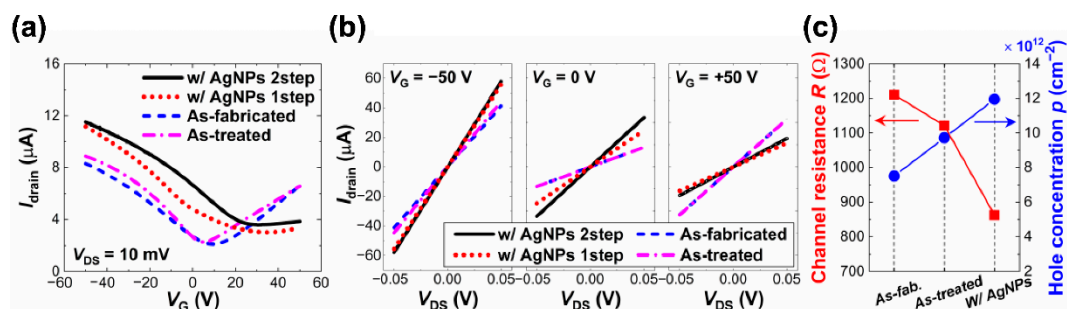


Figure 9. Variations in GFET device characteristics throughout the two-step process. (a) Successive measurements of I_{drain} vs. V_G curves of the GFET at $V_{\text{DS}} = 10 \text{ mV}$ in the three states described previously. (b) Sets of I_{drain} vs. V_{DS} plots of the GFETs in the three states at $V_G = 0$ and $\pm 50 \text{ V}$ for each sample. For the comparison, (a,b) also include the data of dev1 prepared at a P_L value of 5 mW for a τ_L value of 500 ms in Figure 7a,b, respectively, prepared by the one-step process under the same laser conditions. (c) The R and p at $V_G = -50 \text{ V}$ in the three states.

Moreover, the μ_p values of dev3 were $\sim 687.9 \text{ cm}^2/\text{V}\cdot\text{s}$ and $\sim 606.7 \text{ cm}^2/\text{V}\cdot\text{s}$ for the as-fabricated and AgNP-decorated GCs, respectively. Although the amount of AgNPs grown on the GC of dev3 was quite a lot larger than that of dev1 in terms of θ , the μ_p of dev3 decreased much less by $\sim 14.1\%$ through the two-step process than that of dev1 ($\sim 30.7\%$). Probably, the additional focused-laser irradiation in water during the first step may have improved the quality of the AgNPs/GC interface and, hence, alleviated the degradation of μ_p by mitigating the influence of interface scattering into the carrier transport, which is particularly evitable in two-dimensional channel-based devices [55,61–63]. Based on these results, we expect that it would be possible to further enhance the interaction between graphene and AgNPs by optimizing and engineering the laser-assisted PR process.

4. Conclusions

In summary, we demonstrated that a single-layer graphene surface can be decorated area-selectively with AgNPs using the facile one-step focused-laser-assisted PR method and investigated in detail how the formation and growth of AgNPs was affected by the laser-processing parameters. Then, we validated that, based on the GFET device characterization, the selective AgNP decoration on the microscale GFET channel controllably led to p-type doping effects in the graphene. Moreover, we showed that the GFET characteristics could be modulated more substantially with no significant degradation in the carrier mobility in the graphene by carrying out an additional pre-annealing process with a focused-laser beam in advance of the PR process. Therefore, our approach is of relevance to widening the applicability of low-dimensional heterostructures into next-generation electronics and optoelectronics.

Supplementary Materials: The following supporting information can be downloaded at: <https://www.mdpi.com/article/10.3390/nano12203549/s1>, Figure S1: Energy-dispersive X-ray spectroscopy (EDS) elemental mappings of silver nanoparticles (AgNPs) grown on a graphene film (GF) by the photoreduction (PR) process. (a) EDS spectrum acquired from the AgNPs/GF with the inset including the results of elemental composition analysis. (b) Scanning electron microscopy (SEM) image taken under the EDS mode. The set of elemental maps collected from the area of AgNPs/GF shown in (b) for (c) Si K series, (d) O K series, (e) Ag L series, and (f) C K series. For each elemental map, element-rich and element-deficient regions are presented in bright and dark colors, respectively. The signal of Ag element was detected. Further, only the distribution of Ag element in (e) correlates to some degree with the morphology of NPs shown in (b). Therefore, these results suggest that the AgNPs were formed by the PR process; Figure S2: SEM observation of AgNPs grown locally on a GF by the PR process using focused-laser beam. For the focused-laser irradiation, the laser beam diameter and raster step size were $\sim 5\ \mu\text{m}$ and $\sim 20\ \mu\text{m}$, respectively, and the laser powers (P_L) were set at (a,b) 2 mW and (c,d) 5 mW for the two different laser dwell times (τ_L s) of 500 ms and 2000 ms. The diameters of AgNP-coated area were determined to be approximately as small as $\sim 5.22 \pm 0.38\ \mu\text{m}$, $\sim 7.53 \pm 0.27\ \mu\text{m}$, $\sim 9.48 \pm 0.44\ \mu\text{m}$, and $\sim 10.03 \pm 0.91\ \mu\text{m}$ from the SEM images in (a–d), respectively. In these laser process conditions, AgNPs were observed to be formed in a larger area with a higher P_L or a longer τ_L . More importantly, it was shown that the growth area of AgNPs could be localized in the level of the laser beam spot size. All SEM images are presented at the same scale; Figure S3: Representative optical microscopy (OM) images of AgNPs selectively grown on a GF in an area of $50 \times 50\ \mu\text{m}^2$ by the PR process under various laser conditions. The first row of images show the regions of AgNP/GF prepared at the laser powers (P_L s) of (a) 2 mW, (b) 5 mW, (c) 20 mW, and (d) 30 mW for a laser dwell time (τ_L) of 500 ms, while the second row of images display the AgNPs/GF regions given at a fixed P_L of 5 mW for varying τ_L s of (e) 500 ms, (f) 1000 ms, (g) 1500 ms, and (h) 2000 ms. All images are presented at the same scale; Figure S4: Laser processing parameter-dependent morphology characteristics of AgNP grown on GFs and graphene channels (GCs). (a) The surface coverage (θ) and (b) the average particle size (α) of AgNPs on a GF are plotted as a function of P_L at τ_L s of 500 ms and 2000 ms. (c) The θ vs. τ_L and (d) α vs. τ_L plots are also given at P_L s of 2 mW and 5 mW. For the comparison with the θ and α of AgNPs on GCs, the data estimated from the devices (dev1-3) considered in this work are also indicated together. The error bars in (a–d) indicate the standard deviation.

Author Contributions: Conceptualization, C.Y., J.S., S.M.K. and C.K.; formal analysis, I.S., Y.K., M.-K.J. and C.K.; investigation, I.S. and Y.K.; data curation, I.S., Y.K., M.C. and S.K.; methodology, I.S., Y.K. and B.H.L.; project administration, J.S., S.M.K. and C.K.; funding acquisition, J.S. and C.K.; resources, M.-K.J., S.M.K. and C.K.; supervision, C.Y., M.-K.J., J.S., S.M.K. and C.K.; validation, C.Y., M.-K.J., J.S., S.M.K. and C.K.; visualization, I.S., Y.K. and C.K.; writing—original draft, I.S. and C.K.; writing—review and editing, I.S., Y.K., C.Y., M.-K.J., J.S., S.M.K. and C.K. All authors have read and agreed to the published version of the manuscript.

Funding: This research was supported by the Basic Science Research Program through the National Research Foundation of Korea (NRF) funded by the Ministry of Education (NRF-2020R1A4A3079200 & NRF-2020R1C1C1008100).

Data Availability Statement: Not applicable.

Acknowledgments: The authors gratefully acknowledge Eunpa Kim for useful discussion and Yujin Lee, Min Kyung Seong, and Aejin Yang for technical assistance.

Conflicts of Interest: The authors declare no conflict of interest.

References

1. Zhang, Y.; Tan, Y.; Stormer, H.L.; Kim, P. Experimental observation of the quantum Hall effect and Berry's phase in graphene. *Nature* **2005**, *438*, 201–204. [[CrossRef](#)]
2. Bolotin, K.I.; Sikes, K.J.; Jiang, Z.; Klima, M.; Fudenberg, G.; Hone, J.; Kim, P.; Stormer, H.L. Ultrahigh electron mobility in suspended graphene. *Solid State Commun.* **2008**, *146*, 351–355. [[CrossRef](#)]
3. Bunch, J.S.; Verbridge, S.S.; Alden, J.S.; van der Zande, A.M.; Parpia, J.M.; Craighead, H.G.; McEuen, P.L. Impermeable Atomic Membranes from Graphene Sheets. *Nano Lett.* **2008**, *8*, 2458–2462. [[CrossRef](#)] [[PubMed](#)]
4. Lee, C.; Wei, X.; Kysar, J.W.; Hone, J. Measurement of the Elastic Properties and Intrinsic Strength of Monolayer Graphene. *Science* **2008**, *321*, 385–388. [[CrossRef](#)] [[PubMed](#)]

5. Mak, K.F.; Sfeir, M.Y.; Wu, Y.; Lui, C.H.; Misewich, J.A.; Heinz, T.F. Measurement of the Optical Conductivity of Graphene. *Phys. Rev. Lett.* **2008**, *101*, 196405. [\[CrossRef\]](#) [\[PubMed\]](#)
6. Bonaccorso, F.; Sun, Z.; Hasan, T.; Ferrari, A.C. Graphene photonics and optoelectronics. *Nat. Photonics* **2010**, *4*, 611–622. [\[CrossRef\]](#)
7. Dean, C.R.; Young, A.F.; Meric, I.; Lee, C.; Wang, L.; Sorgenfrei, S.; Watanabe, K.; Taniguchi, T.; Kim, P.; Shepard, K.L.; et al. Boron nitride substrates for high-quality graphene electronics. *Nat. Nanotechnol.* **2010**, *5*, 722–726. [\[CrossRef\]](#)
8. Schwierz, F. Graphene transistors. *Nat. Nanotechnol.* **2010**, *5*, 487–496. [\[CrossRef\]](#)
9. Krishna, K.N.I.; Devi, K.M.; Roy Chowdhury, D. Graphene and metal hybridized terahertz metasurfaces toward tunable plasmon-induced transparency effects. *Curr. Appl. Phys.* **2022**, *39*, 158–165. [\[CrossRef\]](#)
10. Stoller, M.D.; Park, S.; Zhu, Y.; An, J.; Ruoff, R.S. Graphene-Based Ultracapacitors. *Nano Lett.* **2008**, *8*, 3498–3502. [\[CrossRef\]](#)
11. Kim, K.S.; Zhao, Y.; Jang, H.; Lee, S.Y.; Kim, J.M.; Kim, K.S.; Ahn, J.; Kim, P.; Choi, J.; Hong, B.H. Large-scale pattern growth of graphene films for stretchable transparent electrodes. *Nature* **2009**, *457*, 706–710. [\[CrossRef\]](#) [\[PubMed\]](#)
12. Shi, J.; Chen, L.; Yang, M.; Mi, Z.; Zhang, M.; Gao, K.; Zhang, D.; Su, S.; Hou, W. Interface contact and modulated electronic properties by external vertical strains and electric fields in graphene/MoS₂ heterostructure. *Curr. Appl. Phys.* **2022**, *39*, 331–338. [\[CrossRef\]](#)
13. Rho, Y.; Lee, K.; Wang, L.; Ko, C.; Chen, Y.; Ci, P.; Pei, J.; Zettl, A.; Wu, J.; Grigoropoulos, C.P. A laser-assisted chlorination process for reversible writing of doping patterns in graphene. *Nat. Electron.* **2022**, *5*, 505–510. [\[CrossRef\]](#)
14. Li, X.; Wang, H.; Robinson, J.T.; Sanchez, H.; Diankov, G.; Dai, H. Simultaneous Nitrogen Doping and Reduction of Graphene Oxide. *J. Am. Chem. Soc.* **2009**, *131*, 15939–15944. [\[CrossRef\]](#)
15. Liu, H.; Liu, Y.; Zhu, D. Chemical doping of graphene. *J. Mater. Chem.* **2011**, *21*, 3335–3345. [\[CrossRef\]](#)
16. Jang, A.; Jeon, E.K.; Kang, D.; Kim, G.; Kim, B.; Kang, D.J.; Shin, H.S. Reversibly Light-Modulated Dirac Point of Graphene Functionalized with Spiropyran. *ACS Nano* **2012**, *6*, 9207–9213. [\[CrossRef\]](#) [\[PubMed\]](#)
17. Kim, S.; Zhao, P.; Aikawa, S.; Einarsson, E.; Chiashi, S.; Maruyama, S. Highly Stable and Tunable n-Type Graphene Field-Effect Transistors with Poly(vinyl alcohol) Films. *ACS Appl. Mater. Interfaces* **2015**, *7*, 9702–9708. [\[CrossRef\]](#)
18. Guo, B.; Liu, Q.; Chen, E.; Zhu, H.; Fang, L.; Gong, J.R. Controllable N-doping of graphene. *Nano Lett.* **2010**, *10*, 4975–4980. [\[CrossRef\]](#)
19. Mamiyev, Z.; Tegenkamp, C. Sn intercalation into the BL/SiC(0001) interface: A detailed SPA-LEED investigation. *Surf. Interfaces* **2022**, *34*, 102304. [\[CrossRef\]](#)
20. Karakachian, H.; Rosenzweig, P.; Nguyen, T.T.N.; Matta, B.; Zakharov, A.A.; Yakimova, R.; Balasubramanian, T.; Mamiyev, Z.; Tegenkamp, C.; Polley, C.M.; et al. Periodic Nanoarray of Graphene pn-Junctions on Silicon Carbide Obtained by Hydrogen Intercalation. *Adv. Funct. Mater.* **2022**, *32*, 2109839. [\[CrossRef\]](#)
21. Lee, J.; Novoselov, K.S.; Shin, H.S. Interaction between Metal and Graphene: Dependence on the Layer Number of Graphene. *ACS Nano* **2011**, *5*, 608–612. [\[CrossRef\]](#) [\[PubMed\]](#)
22. Xu, Z.; Gao, H.; Guoxin, H. Solution-based synthesis and characterization of a silver nanoparticle–graphene hybrid film. *Carbon* **2011**, *49*, 4731–4738. [\[CrossRef\]](#)
23. Shenashen, M.A.; El-Safty, S.; Elshehy, E.A. Synthesis, Morphological Control, and Properties of Silver Nanoparticles in Potential Applications. *Part. Part. Syst. Charact.* **2014**, *31*, 293–316. [\[CrossRef\]](#)
24. Zhang, Z.; Shen, W.; Xue, J.; Liu, Y.; Liu, Y.; Yan, P.; Liu, J.; Tang, J. Recent advances in synthetic methods and applications of silver nanostructures. *Nanoscale Res. Lett.* **2018**, *13*, 54. [\[CrossRef\]](#) [\[PubMed\]](#)
25. Lu, C.; Chen, X. Silver decorated graphene nanocomposites toward electrochemical energy storage. *Chem. Phys. Lett.* **2021**, *771*, 138534. [\[CrossRef\]](#)
26. Xu, G.; Lu, R.; Liu, J.; Chiu, H.; Hui, R.; Wu, J.Z. Photodetection Based on Ionic Liquid Gated Plasmonic Ag Nanoparticle/Graphene Nanohybrid Field Effect Transistors. *Adv. Opt. Mater.* **2014**, *2*, 729–736. [\[CrossRef\]](#)
27. Lee, M.; Lee, K.; Kim, S.; Lee, H.; Park, J.; Choi, K.; Kim, H.; Kim, D.; Lee, D.; Nam, S.; et al. High-Performance, Transparent, and Stretchable Electrodes Using Graphene–Metal Nanowire Hybrid Structures. *Nano Lett.* **2013**, *13*, 2814–2821. [\[CrossRef\]](#)
28. Kim, S.; Jeong, H.; Choi, S.; Park, J. Electrical Conductivity Measurement of Transparent Conductive Films Based on Carbon Nanoparticles. *Coatings* **2019**, *9*, 499. [\[CrossRef\]](#)
29. Wu, T.; Shen, H.; Sun, L.; Cheng, B.; Liu, B.; Shen, J. Facile Synthesis of Ag Interlayer Doped Graphene by Chemical Vapor Deposition Using Polystyrene As Solid Carbon Source. *ACS Appl. Mater. Interfaces* **2012**, *4*, 2041–2047. [\[CrossRef\]](#)
30. You, Z.; Qiu, Q.; Chen, H.; Feng, Y.; Wang, X.; Wang, Y.; Ying, Y. Laser-induced noble metal nanoparticle-graphene composites enabled flexible biosensor for pathogen detection. *Biosens. Bioelectron.* **2020**, *150*, 111896. [\[CrossRef\]](#)
31. Chung, M.G.; Kim, D.; Seo, D.K.; Kim, T.; Im, H.U.; Lee, H.M.; Yoo, J.; Hong, S.; Kang, T.J.; Kim, Y.H. Flexible hydrogen sensors using graphene with palladium nanoparticle decoration. *Sens. Actuators B* **2012**, *169*, 387–392. [\[CrossRef\]](#)
32. Xiao, F.; Song, J.; Gao, H.; Zan, X.; Xu, R.; Duan, H. Coating Graphene Paper with 2D-Assembly of Electrocatalytic Nanoparticles: A Modular Approach toward High-Performance Flexible Electrodes. *ACS Nano* **2012**, *6*, 100–110. [\[CrossRef\]](#)
33. Li, L.; An, B.; Lahiri, A.; Wang, P.; Fang, Y. Doublet of D and 2D bands in graphene deposited with Ag nanoparticles by surface enhanced Raman spectroscopy. *Carbon* **2013**, *65*, 359–364. [\[CrossRef\]](#)

34. Cortijo-Campos, S.; Ramírez-Jiménez, R.; Climent-Pascual, E.; Aguilar-Pujol, M.; Jiménez-Villacorta, F.; Martínez, L.; Jiménez-Riobóo, R.; Prieto, C.; de Andrés, A. Raman amplification in the ultra-small limit of Ag nanoparticles on SiO₂ and graphene: Size and inter-particle distance effects. *Mater. Des.* **2020**, *192*, 108702. [[CrossRef](#)] [[PubMed](#)]
35. Lee, Y.; Kim, E.; Park, Y.; Kim, J.; Ryu, W.; Rho, J.; Kim, K. Photodeposited metal-semiconductor nanocomposites and their applications. *J. Mater. Chem.* **2018**, *4*, 83–94. [[CrossRef](#)]
36. Kim, E.; Ko, C.; Kim, K.; Chen, Y.; Suh, J.; Ryu, S.; Wu, K.; Meng, X.; Suslu, A.; Tongay, S.; et al. Site Selective Doping of Ultrathin Metal Dichalcogenides by Laser-Assisted Reaction. *Adv. Mater.* **2016**, *28*, 341–346. [[CrossRef](#)]
37. Cao, Y.; Gu, M. $\lambda/26$ silver nanodots fabricated by direct laser writing through highly sensitive two-photon photoreduction. *Appl. Phys. Lett.* **2013**, *103*, 213104. [[CrossRef](#)]
38. Samavat, F.; Rahman, J.J. Preparation of silver thin films, and the study of the annealing effects on their structures and optical properties. *Surf. Topogr. Metrol. Prop.* **2015**, *3*, 045003. [[CrossRef](#)]
39. Daeneke, T.; Carey, B.J.; Chrimes, A.F.; Ou, J.Z.; Lau, D.W.M.; Gibson, B.C.; Bhaskaran, M.; Kalantar-zadeh, K. Light driven growth of silver nanoplatelets on 2D MoS₂ nanosheet templates. *J. Mater. Chem. C* **2015**, *3*, 4771–4778. [[CrossRef](#)]
40. Skogerboe, R.K.; Wilson, S. Reduction of ionic species by fulvic acid. *Anal. Chem.* **1981**, *53*, 228–232. [[CrossRef](#)]
41. Yu, Y.; Zhao, Y.; Ryu, S.; Brus, L.E.; Kim, K.S.; Kim, P. Tuning the Graphene Work Function by Electric Field Effect. *Nano Lett.* **2009**, *9*, 3430–3434. [[CrossRef](#)] [[PubMed](#)]
42. Beranek, R. (Photo)electrochemical Methods for the Determination of the Band Edge Positions of TiO₂-Based Nanomaterials. *Adv. Phys. Chem.* **2012**, *2011*, 786759. [[CrossRef](#)]
43. Zhuang, H.L.; Hennig, R.G. Single-Layer Group-III Monochalcogenide Photocatalysts for Water Splitting. *Chem. Mater.* **2013**, *25*, 3232–3238. [[CrossRef](#)]
44. Ferrari, A.C. Raman spectroscopy of graphene and graphite: Disorder, electron–phonon coupling, doping and nonadiabatic effects. *Solid State Commun.* **2007**, *143*, 47–57. [[CrossRef](#)]
45. Das, A.; Pisana, S.; Chakraborty, B.; Piscanec, S.; Saha, S.K.; Waghmare, U.V.; Novoselov, K.S.; Krishnamurthy, H.R.; Geim, A.K.; Ferrari, A.C. Monitoring dopants by Raman scattering in an electrochemically top-gated graphene transistor. *Nat. Nanotechnol.* **2008**, *3*, 210–215. [[CrossRef](#)]
46. Wang, Q.; Li, Y.; Bai, B.; Mao, W.; Wang, Z.; Ren, N. Effects of silicon dioxide surface roughness on Raman characteristics and mechanical properties of graphene. *RSC Adv.* **2014**, *4*, 55087–55093. [[CrossRef](#)]
47. Fregonese, S.; Potereau, M.; Deltimple, N.; Maneux, C.; Zimmer, T. Benchmarking of GFET devices for amplifier application using multiscale simulation approach. *J. Comput. Electron.* **2013**, *12*, 692–700. [[CrossRef](#)]
48. Béraud, A.; Sauvage, M.; Bazán, C.M.; Tie, M.; Bencherif, A.; Bouilly, D. Graphene field-effect transistors as bioanalytical sensors: Design, operation and performance. *Analyst* **2021**, *146*, 403–428. [[CrossRef](#)]
49. Yang, X.; Vorobiev, A.; Yang, J.; Jeppson, K.; Stake, J. A Linear-Array of 300-GHz Antenna Integrated GFET Detectors on a Flexible Substrate. *IEEE Trans. Terahertz Sci. Technol.* **2020**, *10*, 554–557. [[CrossRef](#)]
50. Magdassi, S.; Grouchko, M.; Berezin, O.; Kamyshny, A. Triggering the Sintering of Silver Nanoparticles at Room Temperature. *ACS Nano* **2010**, *4*, 1943–1948. [[CrossRef](#)]
51. Gangwar, M.S.; Agarwal, P. Effect of the annealing temperature on the growth of the silver nanoparticles synthesized by physical route. *AIP Conf. Proc.* **2021**, *2369*, 020100. [[CrossRef](#)]
52. Sachtler, W.M.H.; Dorgelo, G.J.H.; Holscher, A.A. The work function of gold. *Surf. Sci.* **1966**, *5*, 221–229. [[CrossRef](#)]
53. Chelvayohan, M.; Mee, C.H.B. Work function measurements on (110), (100) and (111) surfaces of silver. *J. Phys. C* **1982**, *15*, 2305–2312. [[CrossRef](#)]
54. Takahashi, T.; Tokailin, H.; Sagawa, T. Angle-resolved ultraviolet photoelectron spectroscopy of the unoccupied band structure of graphite. *Phys. Rev. B* **1985**, *32*, 8317–8324. [[CrossRef](#)]
55. Pi, K.; McCreary, K.M.; Bao, W.; Han, W.; Chiang, Y.F.; Li, Y.; Tsai, S.-W.; Lau, C.N.; Kawakami, R.K. Electronic doping and scattering by transition metals on graphene. *Phys. Rev. B* **2009**, *80*, 075406. [[CrossRef](#)]
56. Yan, R.; Zhang, Q.; Li, W.; Calizo, I.; Shen, T.; Richter, C.A.; Hight-Walker, A.R.; Liang, X.; Seabaugh, A.; Jena, D.; et al. Determination of graphene work function and graphene-insulator-semiconductor band alignment by internal photoemission spectroscopy. *Appl. Phys. Lett.* **2012**, *101*, 022105. [[CrossRef](#)]
57. Maiti, R.; Halder, S.; Majumdar, D.; Singha, A.; Ray, S.K. Hybrid opto-chemical doping in Ag nanoparticle-decorated monolayer graphene grown by chemical vapor deposition probed by Raman spectroscopy. *Nanotechnology* **2017**, *28*, 075707. [[CrossRef](#)]
58. Kim, K.; Lee, H.; Johnson, R.W.; Tanskanen, J.T.; Liu, N.; Kim, M.; Pang, C.; Ahn, C.; Bent, S.F.; Bao, Z. Selective metal deposition at graphene line defects by atomic layer deposition. *Nat. Commun.* **2014**, *5*, 4781. [[CrossRef](#)]
59. Jia, Y.; Gong, X.; Peng, P.; Wang, Z.; Tian, Z.; Ren, L.; Fu, Y.; Zhang, H. Toward High Carrier Mobility and Low Contact Resistance: Laser Cleaning of PMMA Residues on Graphene Surfaces. *Nano-Micro Lett.* **2016**, *8*, 336–346. [[CrossRef](#)]
60. Ji, H.; Yi, H.; Seok, J.; Kim, H.; Lee, Y.H.; Lim, S.C. Gas adsorbates are Coulomb scatterers, rather than neutral ones, in a monolayer MoS₂ field effect transistor. *Nanoscale* **2018**, *10*, 10856–10862. [[CrossRef](#)]
61. Chattopadhyay, D.; Queisser, H.J. Electron scattering by ionized impurities in semiconductors. *Rev. Mod. Phys.* **1981**, *53*, 745–768. [[CrossRef](#)]

-
62. McCreary, K.M.; Pi, K.; Swartz, A.G.; Han, W.; Bao, W.; Lau, C.N.; Guinea, F.; Katsnelson, M.I.; Kawakami, R.K. Effect of cluster formation on graphene mobility. *Phys. Rev. B* **2010**, *81*, 115453. [[CrossRef](#)]
 63. Bult, J.B.; Crisp, R.; Perkins, C.L.; Blackburn, J.L. Role of Dopants in Long-Range Charge Carrier Transport for p-Type and n-Type Graphene Transparent Conducting Thin Films. *ACS Nano* **2013**, *7*, 7251–7261. [[CrossRef](#)] [[PubMed](#)]